Comparison and error estimation of 3D fibre orientation analysis of computed tomography image data for fibre reinforced composites

P. Pinter, S. Dietrich, B. Bertram, L. Kehrer, P. Elsner, Kay A. Weidenmann

Pinter, P., S. Dietrich, B. Bertram, L. Kehrer, P. Elsner, and Kay A. Weidenmann. 2018. "Comparison and error estimation of 3D fibre orientation analysis of computed tomography image data for fibre reinforced composites." *NDT & E International* 95: 26–35. https://doi.org/10.1016/j.ndteint.2018.01.001.

Comparison and error estimation of 3D fibre orientation analysis of computed tomography image data for fibre reinforced composites

P. Pinter [a,*], S. Dietrich [a], B. Bertram [a], L. Kehrer [b], P. Elsner [a], K.A. Weidenmann [a]

[a] *Karlsruhe Institute of Technology, Institute for Applied Materials, Karlsruhe, Germany*
[b] *Karlsruhe Institute of Technology, Institute of Engineering Mechanics, Karlsruhe, Germany*

1. Introduction

Fibre reinforced composites have gained increasing importance in the field of semi-structural components in the transportation and automotive industry [1,2]. The goal of mass production in these industries demands for a rigorous process control and validation via non-destructive testing. Therefore, the development of testing strategies and evaluation methods simultaneously allows for a broader application spectrum of composite components and a reproducible and transferable process. Therein the manufacturing process influences the resulting fibre orientation and the architecture significantly. This structure arising due to material flow play a crucial role for an accurate understanding of the materials limitations and advantages. Non-destructive testing provides several tools to investigate fibre orientation distributions and microstructural inhomogenities thereof. Integral methods like ultrasound velocity measurements [3] can usually only determine the overall fibre distribution by an inverse calculation scheme from the elastic properties of the composite. A local resolution and therefore possible changes in fibre orientation across a composite part have to be investigated by imaging techniques like μ-CT [4] thermography [5] or Terahertz spectroscopy [6]. The most efficient and common characterization technique in this respect with a direct 3D measurement of the fibre architecture still is the μ-CT technique. Although investigations of fibre orientation based on 2D images and sectioning of composite parts has been widely used in the past to calculate the 3D orientations via stereological algorithms [7,8], the prevalence of modern μ-CT equipment and 3D visualization software today allows for precise and quick quantitative results.

In general, there are two ways to determine the fibre orientation distribution from volumetric images. On the one hand, the center line of each fibre can be tracked [9]. However, this technique requires images of very high resolution and sufficient contrast. If the material at hand doesn't allow for this mandatory requirements, the algorithm will not be able to track the fibres correctly and results will be erroneous. Nevertheless, it is possible to derive more useful information such as fibre length distribution and a parametrized three-dimensional room curves for each fibre using the fibre tracking approach. On the other hand, the

---

* Corresponding author. Kaiserstr.12, 76131 Karlsruhe, Germany.
E-mail address: pascal.pinter@kit.edu (P. Pinter).

orientation can be computed voxel-based without observing the connectivity using local image features as the three ones compared in the following. These methods have the big advantage that they even allow for evaluating low contrast ct-scans as they result from carbon fibre reinforced polymers. On the downside, those methods don't offer the opportunity to investigate a possible dependency between orientation and fibre length or diameter. The first algorithm in this contribution is based on an anisotropic Gaussian filter and was introduced by Lampert and Wirjadi [10]. Another method described by Daniels et al. [11] in 2007 is based on the Hessian matrix and was used as a second approach. As a last procedure, the structure tensor was implemented. It has already been used for the determination of fibre orientations by Krause et al. [12] in 2010. All methods presented in this contribution are included in Composight [13], which is an open source project developed at the Institute for Applied Materials in Karlsruhe.

In this work, a direct tensor notation is used. Scalars are denoted by lowercase letters, e.g. a, and Vectors by lowercase bold letters, e.g. $\mathbf{a}$. Second-order tensors and fourth-order tensors are indicated by $\mathbf{A}$ and $\mathbb{A}$. The scalar product and the dyadic product are formulated by $\mathbf{A}\cdot\mathbf{B}$ and $\mathbf{A}\otimes\mathbf{B}$. The resulting orientations in each voxel can be used to fit fibre orientation distribution functions (ODF), calculate orientation tensors or even discrete fibre orientation histograms. Regarding engineering applications, the information on the fibre orientation can be used within homogenisation methods in order to predict the effective material behaviour of the composite material. By means of the discrete fibre orientation information, the effective stiffness $\overline{\mathbb{C}}$ is given in terms of the fibre material parameters p_α, the matrix material parameters p_M and the discretely given fibre orientations $\mathbf{n}_\alpha$, i.e.

$$\overline{\mathbb{C}} = \mathrm{f}(p_\alpha, p_M, \mathbf{n}_\alpha). \tag{1}$$

Based on the discretely given μ-CT data, calculations of the effective thermoelastic material properties with the self-consistent scheme (SC), the interaction direct derivative (IDD) or a Hashin-Shtrikman based two-step method are performed in Refs. [14,15].

Moreover, the effective stiffness can be determined with respect to a given fibre orientation distribution function $f(\mathbf{n})$ as

$$\overline{\mathbb{C}} = \mathbb{f}(p_\alpha, p_M, f(\mathbf{n})\,). \tag{2}$$

In case of an empirical orientation density, the orientation distribution function for N orientations reads

$$f(\mathbf{n}) = \frac{1}{N}\sum_{\alpha=1}^{N}\delta(\mathbf{n}-\mathbf{n}_\alpha), \tag{3}$$

where $\delta(\mathbf{n}-\mathbf{n}_\alpha)$ denotes Dirac's delta distribution. For a unit sphere $S := \{\mathbf{n}\in\mathbb{R}^3 : ||\mathbf{n}|| = 1\}$, $\int_S \delta(\mathbf{n}-\mathbf{n}_\alpha)\mathrm{d}S = 1$ holds.

In Ref. [16], fibre orientation distribution functions are estimated based on fibre orientation tensors and combined with the SC and the IDD method for predicting the effective elastic stiffness. Some homogenisation schemes, as the Mori-Tanaka method, cf. [17], provide a direct usage of fibre orientation tensors. Thus, the effective stiffness is calculated by

$$\overline{\mathbb{C}} = \mathbb{f}(p_\alpha, p_M, \mathbf{N}, \mathbb{N}), \tag{4}$$

using the averaged fibre orientation tensors of second and fourth order, $\mathbf{N}$ and $\mathbb{N}$, respectively. In this context, we refer to the fibre orientation tensors of the first kind as defined in Ref. [18] which are discretely given by

$$\mathbf{N} = \frac{1}{N}\sum_{\alpha=1}^{N}\mathbf{n}_\alpha\otimes\mathbf{n}_\alpha, \quad \mathbb{N} = \frac{1}{N}\sum_{\alpha=1}^{N}\mathbf{n}_\alpha\otimes\mathbf{n}_\alpha\otimes\mathbf{n}_\alpha\otimes\mathbf{n}_\alpha. \tag{5}$$

Furthermore, the orientation tensors exhibit all symmetries and $\mathbf{N} = \mathbb{N}[\mathbf{I}]$ holds.

A huge advantage using CT-data for this evaluation is that it is even possible to derive orientation tensors of 4th order directly from the image data. Therefore it is not necessary to make assumptions about suitable closure approximations for modelling mechanical properties of fibre reinforced materials.

2. Materials and methods

2.1. *Artificial test image generation*

Due to the complex fibre architecture in real CT images of non-woven fibre reinforced composites, it is necessary to separate the influential factors on the orientation estimation error. These include the effect of fibre proximity, fibre ends and fibre crossings which can be most easily investigated using artificial fibre images of pairwise fibres. Therefore, we implemented a method based on the Insight Segmentation and Registration Toolkit (ITK) to generate synthetic fibres in an image of size $w\times w\times w$, where w is the edge length of the image in voxels. Variable input parameters are the angle between the fibres θ, the distance d and the number of fibres n (Fig. 1). To prevent a dependency on the discretisation due to the image grid, the coordinate system of Fig. 1 can be tilted in the resulting image. This rotation was applied, because the orientation of a fibre that is perfectly aligned to the grid can easily be determined in comparison to a non-aligned fibre. The tool generates two three-dimensional image files. The first one is a binary image including the fibres. A second one contents vectorial data that describes the real orientation at each voxel. Those files are used to validate the calculated orientations of each method in a following step.

A more application related validation on artificial images is the use of a realistic micro-structure (Fig. 2). Using Geodict®, such images are generated by means of a certain orientation tensor of 2nd order. Three datasets with a size of 500^3 voxels are generated. All fibres have a diameter of 5 voxels and an aspect ratio of 40. The middle and the right image was built with the input orientation tensor $\mathbf{N}_1$ displayed in equation (6).

$$\mathbf{N}_1 = \begin{bmatrix} 0.25 & 0 & 0 \\ 0 & 0.25 & 0 \\ 0 & 0 & 0.5 \end{bmatrix} \tag{6}$$

The middle one includes only straight fibres while the one on the right hand side consists only of curved fibres. The dataset displayed in Fig. 2 (left) includes only unidirectional fibres aligned in x-direction what corresponds to an orientation tensor with $N_{xx} = 1$ while all the other components are zero. All micro structures displayed in Fig. 2 are built with a fibre volume fraction of 5 vol% what corresponds to roughly 12 wt % assuming a glass fibre reinforced composite with a matrix density of $1\,\mathrm{g/cm^3}$ and a fibre density of $2.6\,\mathrm{g/cm^3}$. Moreover, a fourth and fifth fibre architecture using orientation tensor $\mathbf{N}_1$ and straight fibres was

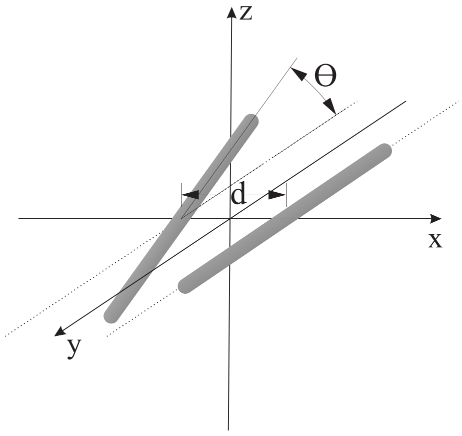

Fig. 1. Displacement and rotation of two fibres.

generated by an algorithm introduced by Schneider [19] for validation at higher fibre contents. The fibre volume fractions of those structures are 13 vol% (approx. 28 wt%) and 20 vol% (approx. 39 wt%).

Since it is hardly possible to generate microstructures with exactly prescribed orientation tensors, GeoDict® returns an achieved tensor after each microstructure generation that is derived from the analytical fibre data. This tensor is also used for the validation of the investigated algorithms for orientation analysis. In GeoDict®, the output of the exact orientation tensor is limited to architectures with straight fibres. However, it is possible to analyse the structures with curved fibres subsequently with tools that are already implemented in GeoDict®. We will use the resulting orientation tensor for comparison even tough it is only an approximation.

2.2. Image acquisition

For tests on real CT images, two different materials were chosen: A 3D printed short fibre reinforced ABS GF10 specimen [20] with a size of 2 mm × 6 mm × 25 mm, because of the good contrast between glass fibres and polymer matrix. Thus, it is possible to separate fibres and matrix easily (Fig. 3 left). Note that the fibre volume content does not have to be correct as we assume to observe the same segmentation bias on each fibre. Due to the printing path, the fibres are mostly aligned in x-direction. The second investigated specimen is a continuous carbon fibre reinforced polymer (CFRP) rod with a diameter of 4 mm manufactured by Carbontec. Its matrix material is epoxy and it contains four carbon fibre rovings which consist of 1200 fibres each. The carbon fibres have very low contrast to the polymer and cannot be separated individually (Fig. 3 right). Both samples were scanned using an Yxlon-CT precision computed tomograph with an open micro-focus X-ray transmission tube with tungsten target and a flat panel detector with 2048 × 2048 pixels from Perkin Elmer.

2.3. Fibre characterization techniques

In the present contribution, all algorithms for the determination of fibre orientations from CT-images work on voxel data without any connectivity. This offers the advantage that it is not necessary to separate fibres and matrix in a pre-processing step or track the centrelines of the fibres. In the following, the discrete three dimensional image data in form of either grey value images or binary data is represented by an image I.

2.3.1. Anisotropic Gaussian filter

Fibre orientation calculations via the anisotropic Gaussian filter was implemented with respect to Lampert and Wirjadi [10]. The image is filtered by an anisotropic Gaussian filter with a certain number of discrete orientations N_G to search for the best matching one. In a first step, the table of orientations to be investigated has to be defined. In the present work, we used a partitioning tool developed by Leopardi [21] to separate one half of the unit sphere in N_G patches of equal area. Subsequently, the algorithm iterates over all listed orientations and applies the anisotropic Gaussian filter. Fig. 4 illustrates the filter using a mask simplified as an ellipsoid. If it is well aligned to a fibre at the present voxel (Fibre A), the filter returns a higher value than for bad aligned orientations (Fibre B). During this procedure, two values are stored in each voxel: The highest filter response that appeared in all orientations

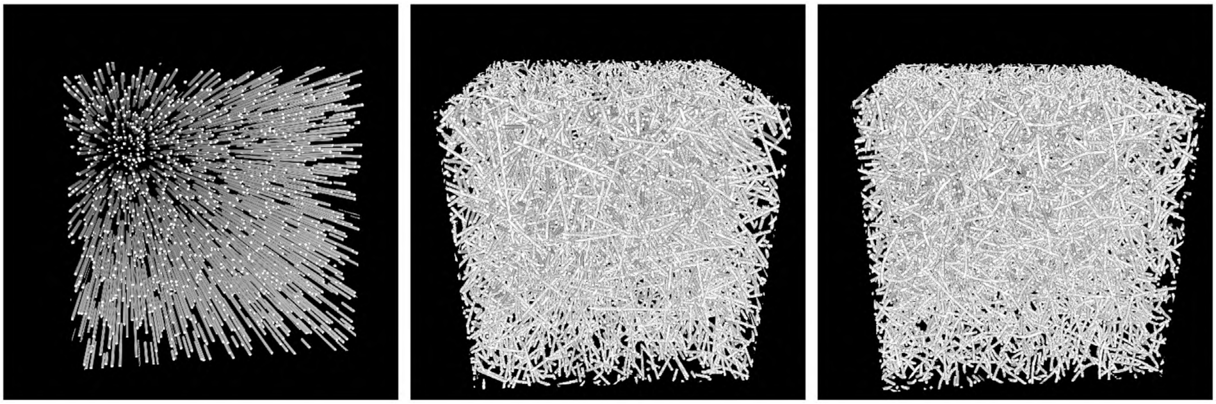

Fig. 2. Artificial images generated with GeoDict®. The input orientation tensor was chosen to $N_{xx} = 0.25$, $N_{yy} = 0.25$ and $N_{zz} = 0.5$. Left: Unidirectional fibres. Middle: Fibre architecture with straight fibres. Right: Fibre architecture with curved fibres.

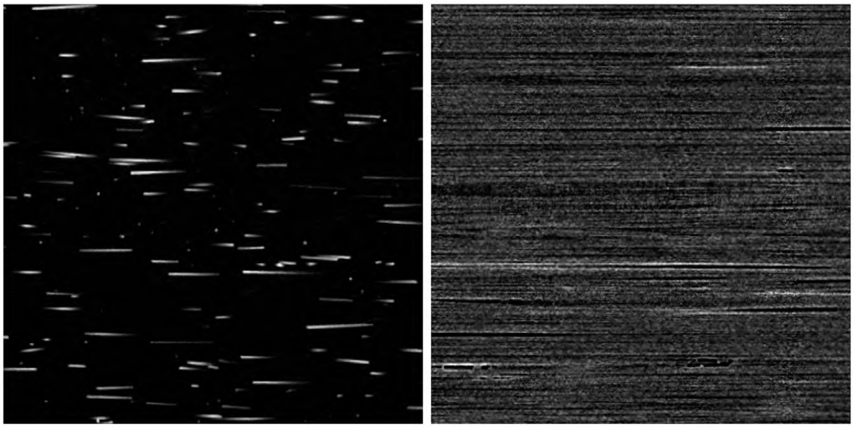

Fig. 3. CT-Scan of 3D printed ABS GF 10 specimen (left) and the unidirectional continuous carbon fibre reinforced specimen (right).

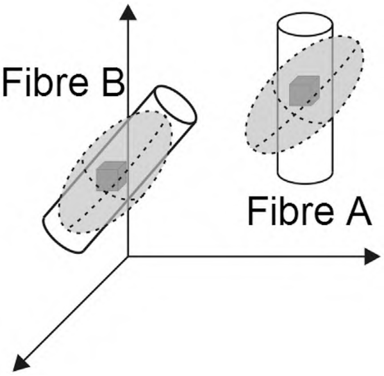

Fig. 4. Schematic representation of the Gaussian filter.

investigated, and the corresponding line number of the orientation table. Latter is the result of the algorithm and is stored as an integer image. Actually due to computational efficiency, the image is rotated and filtered with a recursive Gaussian filter subsequently for each direction instead of rotating the filter mask. Since the error of the calculation with straight fibres could be reduced by choosing a high aspect ratio, it was set to two ($\sigma_x = 2\sigma_y = 2\sigma_z$) with respect to [10]. Due to the fixed aspect ratio, the smaller principal axis (σ_z and σ_y) will only be termed as σ in the following. Furthermore, the number of examined angles is set to $N_G = 100$ on the half sphere for investigations that are carried out within this contribution.

2.3.2. Hessian matrix

The discrete Hessian Matrix (7) can be used to calculate local orientations [11] since it describes the curvature of the surrounding grey values. First, the initial image is processed by a Gaussian filter to receive a blurred image I_σ. This step is crucial for binary images, because gradients have to be generated in the inside of the fibres (Fig. 5). After blurring, the Hessian Matrix is computed in each voxel and due to the symmetry, only six of nine values have to be stored. Finally, an eigenvalue analysis is applied while the eigenvector corresponding to the smallest eigenvalue is assigned as orientation on the present position. This vectors are written to the resulting image as floating point values.

$$\nabla^2 I_\sigma(\mathbf{x}) \,\widehat{=}\, \begin{bmatrix} \frac{\partial^2 I_\sigma}{\partial x^2} & \frac{\partial^2 I_\sigma}{\partial x \partial y} & \frac{\partial^2 I_\sigma}{\partial x \partial z} \\ \frac{\partial^2 I_\sigma}{\partial y \partial x} & \frac{\partial^2 I_\sigma}{\partial y^2} & \frac{\partial^2 I_\sigma}{\partial y \partial z} \\ \frac{\partial^2 I_\sigma}{\partial z \partial x} & \frac{\partial^2 I_\sigma}{\partial z \partial y} & \frac{\partial^2 I_\sigma}{\partial z^2} \end{bmatrix} \tag{7}$$

2.3.3. Structure tensor

Local orientation analysis using the structure tensor [12,22] is a very robust approach. It is based on the first numerical derivative (Fig. 6 (a)) of the image, which is computed in a combination with a Gaussian blur of a width of σ. Subsequently, the dyadic product of the present gradient (Eq. (8)) can be built in each voxel.

$$\nabla I_\sigma(\mathbf{x}) \otimes \nabla I_\sigma(\mathbf{x}) \,\widehat{=}\, \begin{bmatrix} \left(\frac{\partial I_\sigma}{\partial x}\right)^2 & \frac{\partial I_\sigma}{\partial x}\frac{\partial I_\sigma}{\partial y} & \frac{\partial I_\sigma}{\partial x}\frac{\partial I_\sigma}{\partial z} \\ \frac{\partial I_\sigma}{\partial y}\frac{\partial I_\sigma}{\partial x} & \left(\frac{\partial I_\sigma}{\partial y}\right)^2 & \frac{\partial I_\sigma}{\partial y}\frac{\partial I_\sigma}{\partial z} \\ \frac{\partial I_\sigma}{\partial z}\frac{\partial I_\sigma}{\partial x} & \frac{\partial I_\sigma}{\partial z}\frac{\partial I_\sigma}{\partial y} & \left(\frac{\partial I_\sigma}{\partial z}\right)^2 \end{bmatrix} \tag{8}$$

Every tensor determined this way can be interpreted as a line with a certain orientation which is perpendicular to the fibre surface (Fig. 6 (b)) or the gradient at the present voxel, respectively. In order to receive the fibre orientation, all tensors are averaged by a Gaussian blur - denoted as function $G(I,\rho)$ in Eq. (9) - with the standard deviation ρ. This blurring parameter has to be larger than the first one that is used for the derivative. It represents the image region that is taken into account to determine an orientation at a certain point.

$$\mathbf{J}_{\boldsymbol{\rho}}(\mathbf{x}) = G(\nabla I_\sigma(\mathbf{x}) \otimes \nabla I_\sigma(\mathbf{x}), \rho) \tag{9}$$

For the case of a fibre, it results in a structure tensor with mostly flat representation surfaces which are aligned perpendicular to the local fibre orientation (Fig. 6 (c)). Using this tensor, the fibre orientation can be calculated by evaluating the smallest eigenvalue of the tensor and its corresponding eigenvector (Fig. 6 (d)).

2.4. Error criterions

For the rating of the three fibre characterization techniques mentioned above, there is a need of an error criterion that respects the distance as well as the angle of the fibres. This criterion is used both to determine the optimal parameters for each orientation algorithm and to compare the algorithms to each other based on the results from the artificial images with only two fibres. In a first step, the error of each voxel described by the spatial angle between real and evaluated orientation, in a single image is summed up and divided by the number of existent fibre voxels. In fact, θ_E cannot be larger than 90° what implies that the global error within the entire image is $0 \le \theta_{gE} \le 90$.

$$\theta_{gE}(I(\alpha, d)) = \sum_{i=1}^{N} \frac{\theta_{E,i}}{N_{white}} \tag{10}$$

According to this global error for a single image, the next step is to

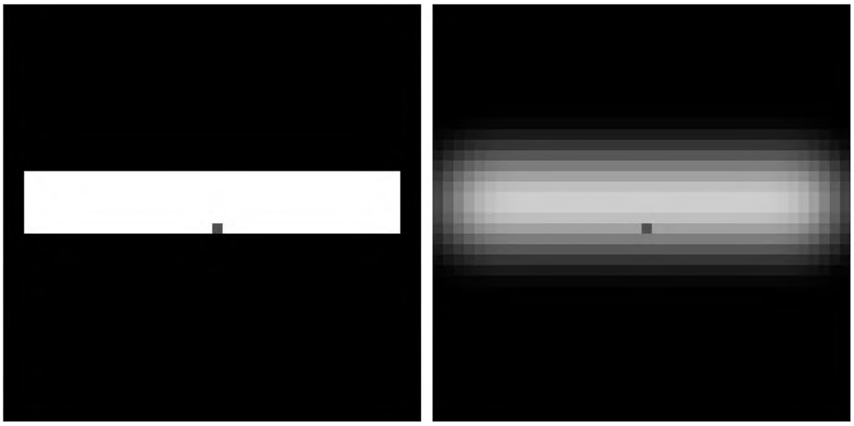

Fig. 5. Two dimensional image of a binarized fibre (left) and blurred with a Gaussian filter (right).

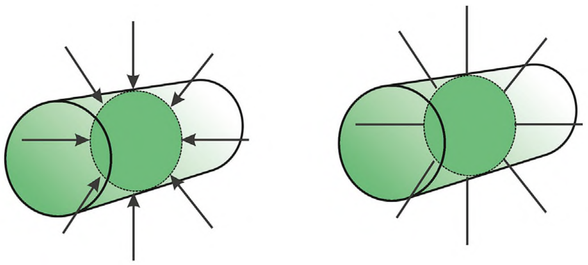

(a) Image gradients

(b) Tensor resulting from dyadic product of gradient

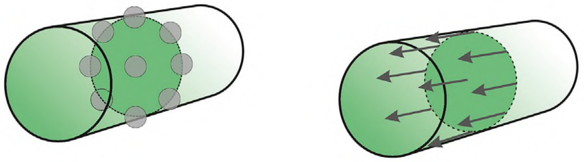

(c) structure tensor: Blurred tensors within an image region

(d) Orientations derived from averaged structure tensors

Fig. 6. Determining the fibre orientation using the structure tensor.

calculate a fibre architecture dependent error for a set of distances and angles to evaluate a measure that describes the quality of each algorithm for a specific diameter. Eq. (11) shows the principle of the fibre architecture dependent error E_A, where N_α and N_d are the total number of investigated angles and distances. With this scheme, it is also possible to test the algorithms for certain configuration that describes e.g. unidirectional fibres by using just an angle of zero degree.

$$E_A = \sum_{i=1}^{N_\alpha} \sum_{j=1}^{N_d} \frac{\theta_{gE}\left(I\left(\alpha_i, d_j\right)\right)}{N_\alpha \cdot N_d} \tag{11}$$

The performance of the different methods on artificial fibre architectures generated by GeoDict® were compared by the Frobenius norm of the differences of input and output orientation tensors ($\mathbf{N}_I$ and $\mathbf{N}_O$). Note that this error E_T does not describe an angle and thus it is not comparable with E_A from the experiments with only two fibres.

$$E_T = \frac{\| \mathbf{N}_I - \mathbf{N}_O \|_F}{\| \mathbf{N}_I \|_F} \tag{12}$$

3. Results

3.1. Artificial images of pairwise fibres

This first investigation with only two fibres per image was carried out to find optimal input parameters for each method by an exhaustive grid search. Artificial fibre configurations were built with fibre diameters of five and ten voxels. The angle was varied from zero to 90° in ten steps. Furthermore, the fibre distance was chosen from one time the diameter - what results in an image with touching fibres - up to two times the diameter. This experimental matrix was evaluated with each method and different input parameters to determine E_A and find the best input parameters for each algorithm.

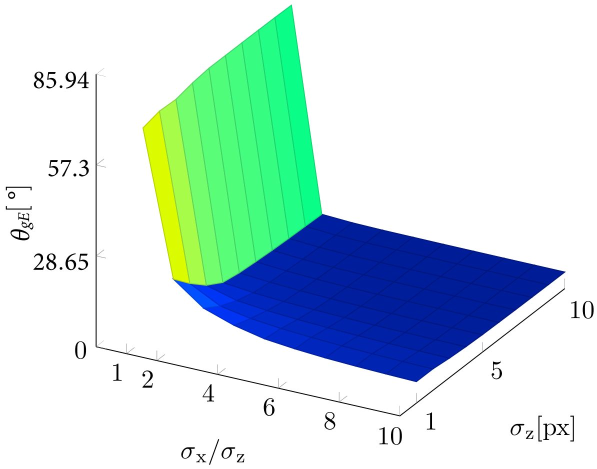

Fig. 7. Angular Error using different values for σ and varying aspect ratios of the anisotropic Gaussian filter on artificial images with a single fibre of 10 voxels in diameter.

3.1.1. Anisotropic Gaussian filter

As mentioned above, the error of this method will decrease with higher aspect ratios of the filter. This circumstance is illustrated in Fig. 7 on artificial images with a single fibre. However, due to the reasons mentioned before the following tests are carried out with an aspect ratio of two.

Fig. 8 shows the fibre architecture dependent errors for fibres with a diameter of five and ten voxels. It can be seen that the optimum for σ for a diameter of five voxels is at $\sigma = 3$ voxels with an absolute angular error of $E_A = 8.48°$. The best results at a fibre diameter of ten voxels are obtained at $\sigma = 6$ voxels with (see Fig. 9)$E_A = 8.19°$.

3.1.2. Hessian matrix

The same experiment using the Hessian matrix resulted in an overall error of 10.31° both for diameters of 5 and 10 voxels. This minimum was observed for $\sigma = 6$ voxels with a diameter of ten voxels. For the 5 voxels thin fibres, the optimum was found in a very sharp local minimum and thus the calculation was repeated on a finer grid and resulted in $\sigma = 2.9$ voxels (Fig. 10).

3.1.3. Structure tensor

Since there are two input parameters necessary for the structure tensor, the optimum is searched in a two dimensional space. Therefore, the results are shown in contour plots (Fig. 11) while the minimum values for E_A are marked with a red dot. Tests with a fibre diameter of ten voxels showed that the first blurring parameter σ has to be chosen very small and should be set to values around one voxel to get a good result. The second parameter for the averaging of the structure tensor on a larger scale (cf. Fig. 6) has its optimum at $\rho = 6$ voxels. The investigation of the fibres with a diameter of 10 voxels was carried out once again since the optimum was found at the border of the diagram. Fig. 12 shows the same diagram with a finer resolution around the optimum. Within this figure, the minimum was detected at $\sigma = 0.8$ voxels and $\rho = 5.6$ voxels with $E_A = 1.68°$.

3.2. Artificial micro structure images

The three different methods led to the errors E_T displayed in Table 1

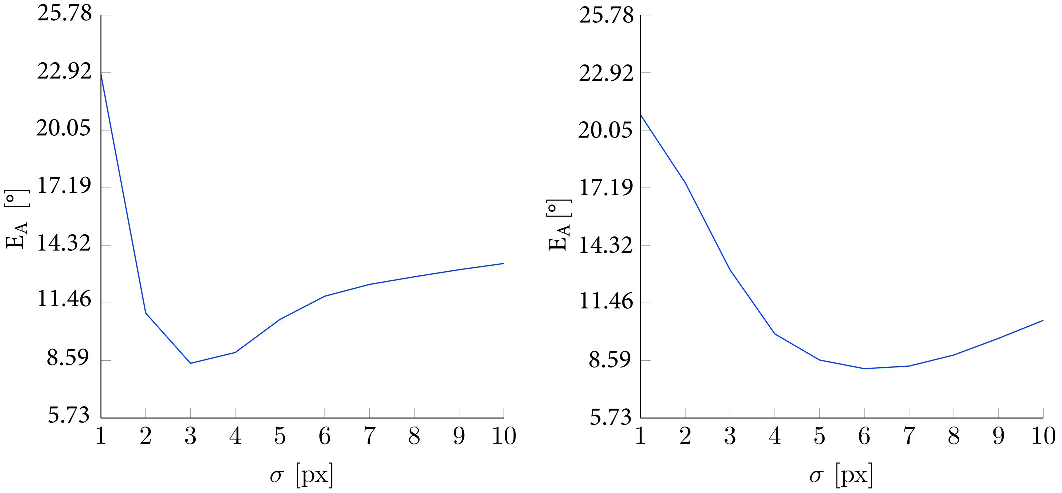

Fig. 8. E_A of fibres with a diameter of 5 voxels (left) and 10 voxels (right) using the method based on the anisotropic Gaussian filter.

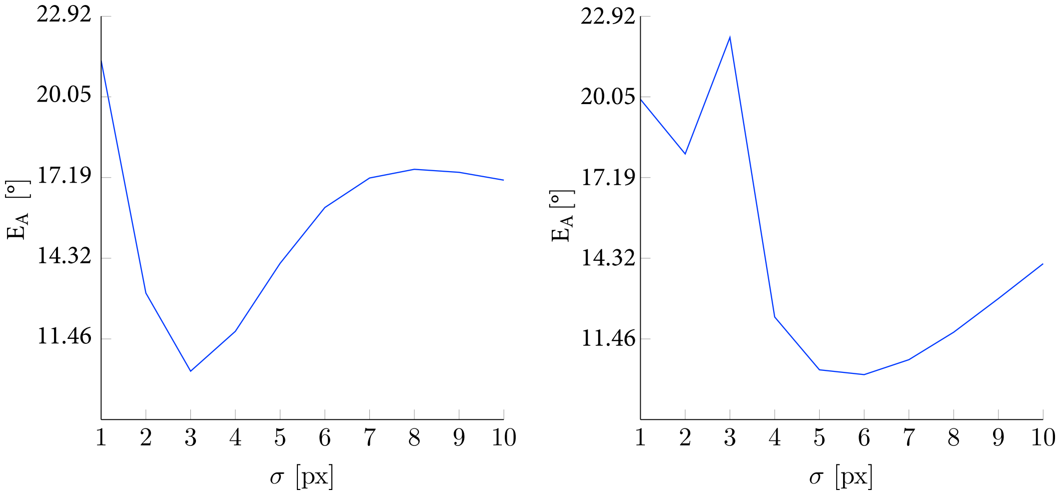

Fig. 9. E_A of fibres with a diameter of 5 voxels (left) and 10 voxels (right) using the method based on the Hessian matrix.

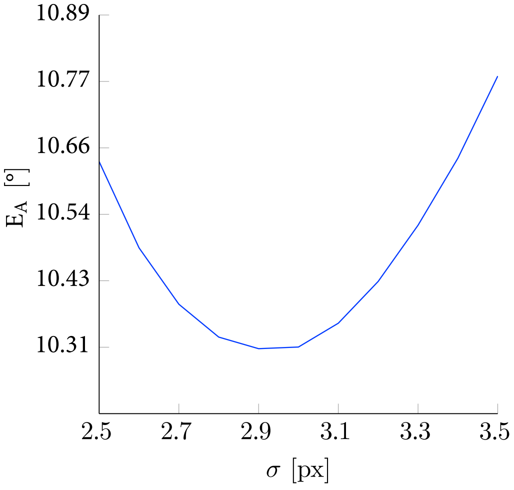

Fig. 10. E_A of fibres with a diameter of 5 voxels using the method based on the Hessian matrix on a finer grid.

for the artificial microstructures. The following input parameters were chosen for the calculation:

- Gaussian filter: $\sigma = 3$ voxels
- Hessian Matrix: $\sigma = 3$ voxels
- Structure Tensor: $\sigma = 0.8$ voxels, $\rho = 3$ voxels

Computation times and memory consumption for the artificial structures with a size of 500^3 voxels and a bit depth of 16 bit are listed in Table 2. For larger images, time scales nearly linear with the image size. Calculations were carried out on a 16-core Intel Xeon E5-2620 v4 workstation with 256 GB RAM.

3.3. Orientation analysis of real CT-Scans

Investigations on real CT-scans of 3D printed fibre reinforced polymers resulted in orientation tensors shown in Table 3. Since the fibre diameter was estimated to 4 voxels in the raw image (Fig. 3), the input parameters were set to:

- Gaussian filter: $\sigma = 2$ voxels

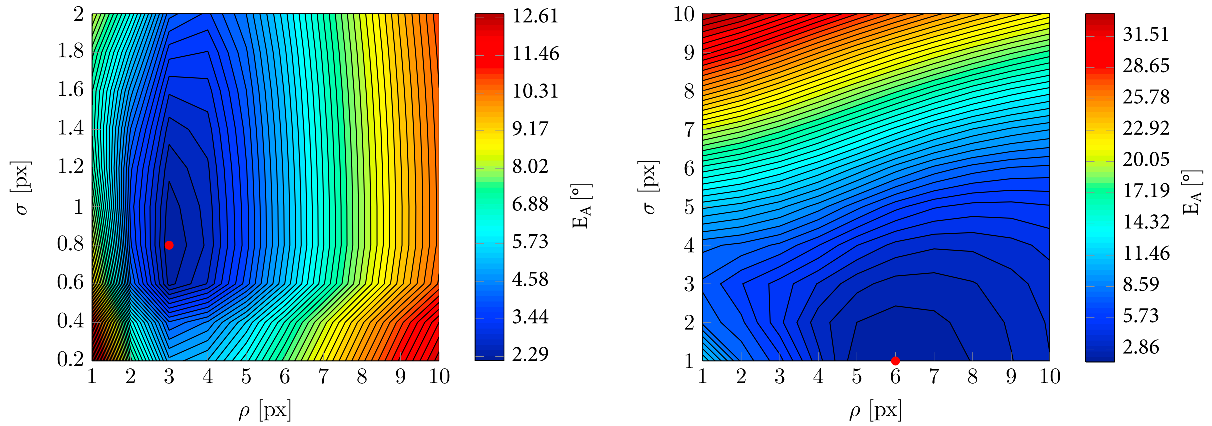

Fig. 11. E_A of fibres with a diameter of 5 voxels (left) and 10 voxels (right) using the method based on the structure tensor. The smallest error is marked by the red dot. (For interpretation of the references to colour in this figure legend, the reader is referred to the Web version of this article.)

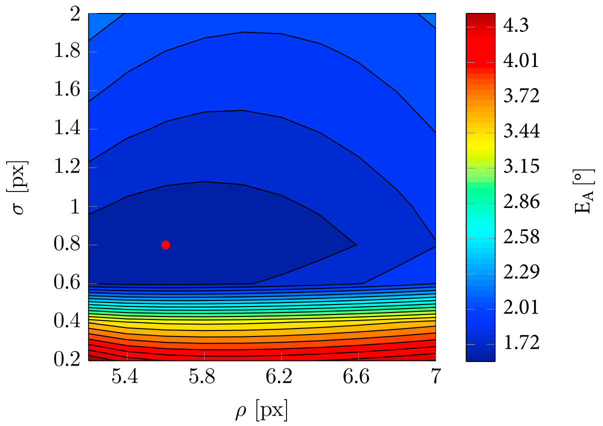

Fig. 12. E_A of fibres with a diameter of 5 voxels using the method based on the structure tensor on a finer grid.

Table 1
Error E_T of artificial images from GeoDict®.

Method	UD-Fibres	Straight Fibres	Straight Fibres	Straight Fibres	Curved Fibres
	5 vol%	5 vol%	13 vol%	20 vol%	5 vol%
Anisotropic Gaussian Filter	0.0110	0.0614	0.0248	0.1116	0.1920
Hessian Matrix	0.0417	0.0277	0.0500	0.2122	0.0050
Structure Tensor	0.0014	0.0033	0.0377	0.0430	0.0238

Table 2
Computation times for artificial images with a size of 500^3 voxels and a bit depth of 16bit.

Method	Computation Time	Memory Consumption
Anisotropic Gaussian Filter	16 min 40 s	6 GB
Hessian Matrix	1 min 58 s	8 GB
Structure Tensor	2 min 2 s	8 GB

- Hessian Matrix: $\sigma = 2$ voxels
- Structure Tensor: $\sigma = 0.2$ voxels, $\rho = 2$ voxels

Table 3
Orientation Tensors derived from 3D-printed glass fibre reinforced specimen.

Anisotropic Gaussian Filter $\mathbf{N}_G$	0.9204	0.0106	0.0036
	0.0106	0.0360	0.0001
	0.0036	0.0001	0.0436
Hessian Matrix $\mathbf{N}_H$	0.9270	−0.0013	0.0145
	−0.0013	0.0311	0.0006
	0.0145	0.0006	0.0419
Structure Tensor $\mathbf{N}_{ST}$	0.9658	−0.0019	0.0207
	−0.0019	0.0069	0.0002
	0.0207	0.0002	0.0273

Table 4
Orientation Tensors derived from unidirectional carbon fibre reinforced polymer rod.

Anisotropic Gaussian Filter $\mathbf{N}_G$	0.3460	−0.0003	−0.0072
	−0.0003	0.3572	−0.0024
	−0.0072	−0.0024	0.2968
Hessian Matrix $\mathbf{N}_H$	0.2588	0.0002	0.0000
	0.0002	0.3720	0.0052
	0.0000	0.0052	0.3693
Structure Tensor $\mathbf{N}_{ST}$	0.9977	−0.0039	0.0009
	−0.0039	0.0011	0.0002
	0.0009	0.0002	0.0012

The results of unidirectional carbon fibre reinforced polymers are shown in Table 4. Note that the fibres could not be separated from the matrix and thus every voxel was taken into account to determine the orientation tensor. For this test, the input parameters of the different methods were chosen as followed:

- Gaussian filter: $\sigma = 1$ voxels
- Hessian Matrix: $\sigma = 2$ voxels
- Structure Tensor: $\sigma = 0.2$ voxels, $\rho = 4$ voxels

4. Discussion

4.1. *Artificial images of pairwise fibres*

Comparing the results from the first test (Table 5) it is obvious that the structure tensor based method offers the most precise data. Note that the processed configurations of angles and diameters are evenly distributed from 0° to 90° and from one fibre diameter up to two times the diameter.

Even if the resulting error of the orientation analysis based on the Hessian matrix and the anisotropic Gaussian filter is higher than the structure tensor based method, those methods can offer some advantages. The algorithm based on the anisotropic Gaussian filter requires least working memory as it is not necessary to process a symmetric tensor with six independent floating-point variables. However, it is the slowest method due to the many image rotations that have to be applied. The

Table 5
Fibre architecture dependent error E_A resulting from investigated methods with different fibre diameters.

Method	10 voxels diameter	5 voxels diameter
Anisotropic Gaussian Filter	8.19°	8.48°
Hesse-Matrix	10.31°	10.31°
Structure Tensor	1.68°	2.18°

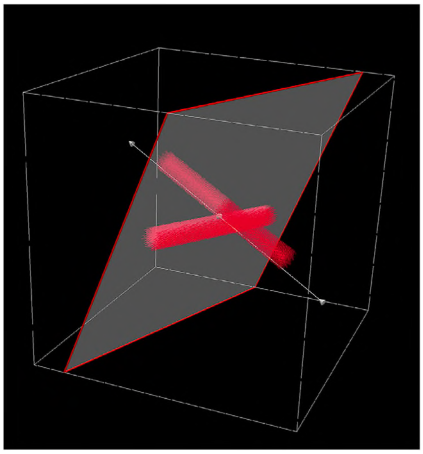

Fig. 13. 3D-representation of the cutting plane through the cross section area which is illustrated in the following pictures.

error could eventually be reduced by a increasing number of angles that are examined. Nevertheless, the computing time will rise with this number, too.

In order to locate the resulting misalignments within the processed images, a slice through the two touching fibres with a diameter of 10 voxels and an angle of 70° according to Fig. 13 is generated. Figs. 14–16 show those planes as glyph plots, where every dash represents the orientation that was determined in the present voxel by the different methods using optimal input parameters. Fig. 14 shows that the anisotropic Gaussian filter generates errors mainly in the cross section area, but even at the fibre ends. It is easy to suggest the origin of the errors for this method: If the elliptic filter mask is placed in the cross section area, the filter response is higher for the rotated case, because the intersection of the filter with the white areas is larger.

Fig. 15 shows the resulting slice for the Hessian matrix based method. There are high misalignments at the cross section as well as at the fibre ends. These erroneously estimated orientations are caused by the Gaussian blur that has to be applied in advance to orientation analysis. In the present image, the input parameter was chosen to $\sigma = 6$. Nevertheless, the filter influences also voxels with larger distances, as it is calculated by a recursive infinite impulse response filter [23]. On real CT scans, the blurring parameter could be reduced due to the image gradient that is already present within the fibres due to the limited resolution and other effects resulting from the reconstruction. However, real images are also affected by noise which influences the second derivative of the image significantly and thus the blurring is still necessary.

The structure tensor leads to the best results on artificial test data with two fibres. In Fig. 16 it is hardly possible to find misoriented dashes. However, in the cross section area there are some small errors in form of a continuous cross-fading of the orientations from one fibre orientation to the other, which can not be recognised in the present view. Nevertheless, those inaccurate estimated orientations at the crossing disappear almost entirely at small fibre distances compared to the other methods. At the fibre ends, there are only very slight differences in orientation.

In the following, the effect of the previously discussed error E_A caused by the fibre architecture on the calculated material properties is investigated. For this purpose, the effective elastic stiffness is calculated for a mechanical model containing artificial unidirectional fibres embedded in a polymer matrix material. In this context, the Mori-Tanaka homogeni-

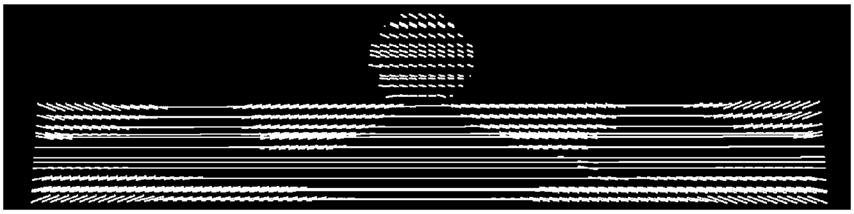

Fig. 14. Cross section area of two fibres with an angle of 70° processed by the anisotropic Gaussian filter.

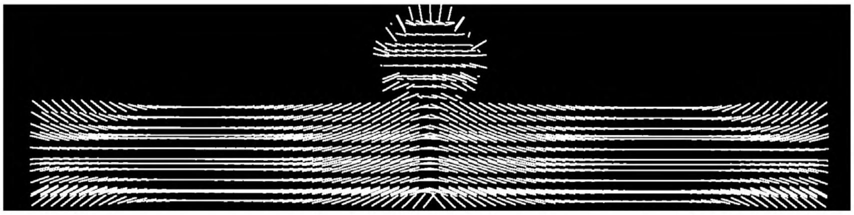

Fig. 15. Cross section area of two fibres with an angle of 70° processed by the method based on the Hessian Matrix.

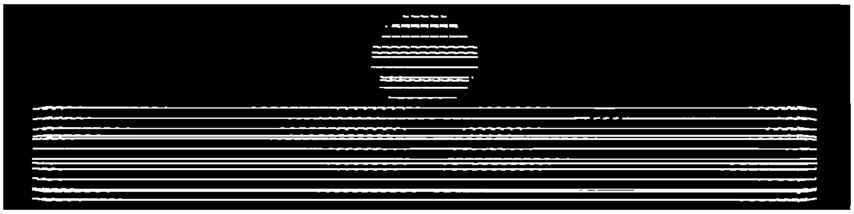

Fig. 16. Cross section area of two fibres with an angle of 70° processed by the method based on the structure tensor.

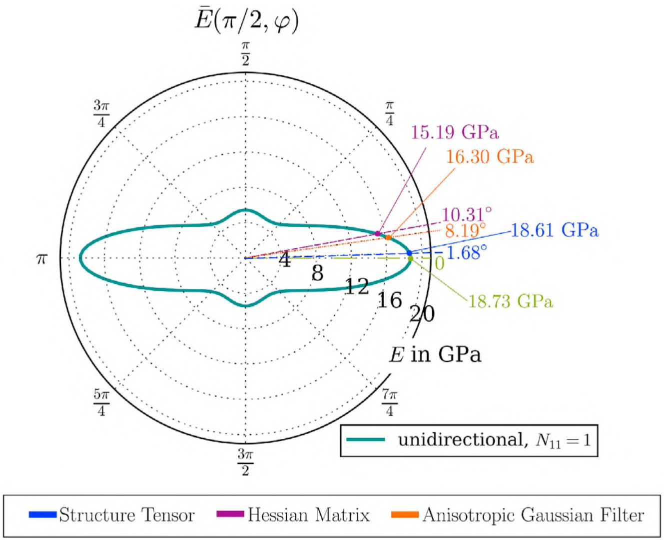

Fig. 17. Polar plot of the Young's modulus of a unidirectional glass fibre reinforced Polymer.

sation [24] is used, formulated in terms of orientation tensors of second and fourth order, cf. e.g. Ref. [25]. Assuming isotropic and piecewise constant material properties of the constituents, Young's modulus and Poisson's ratio of the matrix material are chosen to be $E_M = 3.4$ GPa and $\nu_M = 0.22$, respectively. Regarding the fibre material, Young's modulus $E_F = 73.0$ GPa and Poisson's ratio of $\nu_F = 0.385$ serve as input for the simulation method. The simulated fibres exhibit a length of $l_F = 2500\ \mu$m and a diameter of $d_F = 10\ \mu$m. With respect to a micro structure with unidirectional fibres, the orientation tensors of second and fourth order read

$$\boldsymbol{N} \mathrel{\widehat{=}} \begin{bmatrix} 1 & 0 & 0 \\ 0 & 0 & 0 \\ 0 & 0 & 0 \end{bmatrix}, \quad \mathbb{N} \mathrel{\widehat{=}} \begin{bmatrix} 1 & 0 & 0 & 0 & 0 & 0 \\ 0 & 0 & 0 & 0 & 0 & 0 \\ 0 & 0 & 0 & 0 & 0 & 0 \\ 0 & 0 & 0 & 0 & 0 & 0 \\ 0 & 0 & 0 & 0 & 0 & 0 \\ 0 & 0 & 0 & 0 & 0 & 0 \end{bmatrix}. \tag{13}$$

The orientation-dependent effective Young's modulus $\overline{E}$ is determined by

$$\overline{E}(\boldsymbol{d}) = \left(\boldsymbol{d} \otimes \boldsymbol{d} \cdot \overline{\mathbb{C}}^{-1}[\boldsymbol{d} \otimes \boldsymbol{d}]\right)^{-1}, \tag{14}$$

with the effective stiffness $\overline{\mathbb{C}}$ and $\boldsymbol{d}$ parametrized in spherical coordinates, cf. [26] Fig. 17 illustrates $\overline{E}(\boldsymbol{d})$ in the *x-y* plane. Table 5 lists the error E_A in dependence of the fibre architecture for a fibre diameter of 10 voxels regarding the three different methods. The listed angles represent the error range of the mentioned methods. In order to determine the impact on the effective Young's modulus, the values at the angles 8.18°, 10.31° and 1.68° are marked in Fig. 17 indicating the corresponding method. The values for the effective Young's modulus at these angles, referred to the value in fibre direction, i.e.0°, give the quantitative error for the selected methods. While the value for the Young's modulus in 0° direction reads 18.73 GPa, the maximum deviation is 15.19 GPa in case of using method based on the Hessian matrix leading to a percentage error of 18.9%. The method based on the anisotropic Gaussian filter leads to a relative error of 13%, while the algorithm using the structure tensor shows a deviation of only 0.6%.

4.2. *Artificial micro structure images*

Validation of the algorithms using artificial micro structures offer a more application related measure than models with only two fibres. Table 1 shows minor errors E_T for the unidirectional configuration with all methods while the structure tensor leads to the best results. For a fibre orientation distribution derived from the orientation tensor mentioned in equation (6) at different fibre contents, the structure tensor leads to the best results. This is in accordance with the investigations of the two fibre models. The method based on the Hessian matrix resulted in a better value for curved fibres. In contrast to the straight structures, there was no orientation tensor that was derived directly from the analytical data in GeoDict®. Thus, the orientation tensor that was used for the validation had to be calculated subsequently using algorithms that work similar than those presented in this contribution. Due to this reason, the error derived from this data does not show the absolute error but only a comparison to another approach. Nonetheless, E_T is relatively small for the methods based on the Hessian matrix and the structure tensor and thus it can be assumed that the methods work reliable on perfectly binarized images like those that result from GeoDict®. Computation time was almost equal for Hessian matrix and structure tensor, but around eight times as high as with the anisotropic Gaussian filter. Note that none of the algorithms was optimized with respect to the computation time.

4.3. *Orientation analysis of real CT-Scans*

Since the scans of the glass fibre reinforced 3D-printed specimen can be separated easily, only fibre voxels were taken into account for the estimation of the orientation tensor. Therefore, the same grey value threshold was used according to the Renyi Entropy [27] for each algorithm. As it can be seen in Table 3, the orientation tensors appear to be quite similar, while the structure tensor shows the highest value in x-direction. Nevertheless, the correct orientation tensor is not known and accordingly it is not possible to give evidence about the quality of the different methods. Due to the very similar results in this test, it can be stated that all methods work quiet well on real scans with moderate fibre content that can be separated by a grey level threshold.

In contrast to this easily processable image, the orientation analysis of the unidirectional carbon fibre reinforced specimen is a greater challenge. As it is not possible to see single fibres in the image, the algorithm for analysis has to be extremely robust. Observing the results in Table 4, only the structure tensor based method leads to an orientation tensor with a preferred *x*-orientation and thus a high value in N_{xx}. The other methods resulted in tensors without any preferred orientation that is worth mentioning. Even higher and lower blurring parameters for the anisotropic Gaussian filter and the Hessian matrix were observed, but none of them resulted in an anisotropic orientation tensor. The signal to noise ratio of those images is too low for the application of the second numerical derivative for fibre orientation analysis.

5. Conclusions

Experiments with two artificial fibres showed that there is an optimal parameter set in dependence of the fibre diameter for each algorithm. The structure tensor offered the best results on this kind of data. The newly acquired knowledge about the parameter settings was transferred and validated on full size images of artificial fibre architectures with known orientation tensors and real images. The artificial images and CT scans of glass fibre reinforced polymers showed that even for this type of data, the structure tensor based method has the best performance for most structures. Furthermore, low contrast pictures from carbon fibre reinforced polymers could only be processed by the structure tensor based method while the other algorithms did not result in an orientation tensor with any preferred orientation. If images can be separated and the resolution is sufficient, the methods based on the anisotropic Gaussian filter can be a good alternative. It requires least working memory of all compared methods, but depending on the number of quantified angles, the computational time is much higher. The algorithm using the Hessian matrix is very sensitive to noise and even on images with high contrast and resolution, the error can be relatively high due to the large regions of misalignment in cross-section areas and fibre ends. In summary, it can be stated that the structure tensor based method is the most flexible and robust method for orientation analysis. Even low contrast images - where single fibres are indistinguishable - can be analysed reliably.

Acknowledgments

The research documented in this manuscript has been funded by the German Research Foundation (DFG) within the International Research Training Group Integrated engineering of continuous-discontinuous long fibre reinforced polymer structures (GRK 2078). The support by the German Research Foundation (DFG) is gratefully acknowledged. Furthermore, we like to thank Robert Bertoti from the Institute for Engineering Mechanics in Karlsruhe for valuable Discussions.

References

[1] Holbery James, Houston Dan. Natural-fiber-reinforced polymer composites in automotive applications. Jom 2006;58(11):80–6.
[2] Schut JH. Long-fiber thermoplastics extend their reach. Plast Technol 2003;49(4): 56–61.
[3] Dunn Martin L, Ledbetter Hassel. Estimation of the orientation distribution of shortfiber composites using ultrasonic velocities. J Acoust Soc Am 1996;99(1): 283–91.
[4] Shen Hongbin, Nutt Steven, Hull David. Direct observation and measurement of fiber architecture in short fiber-polymer composite foam through micro-ct imaging. Compos Sci Technol 2004;64(13–14):2113–20.
[5] Schroeder JA, Ahmed T, Chaudhry B, Shepard S. Non-destructive testing of structural composites and adhesively bonded composite joints: pulsed thermography. Compos A Appl Sci Manuf 2002;33(11):1511–7.
[6] dens Jr C, Scheller M, Wietzke S, Romeike D, Jansen C, Zentgraf T, et al. Terahertz spectroscopy to study the orientation of glass fibres in reinforced plastics. Compos Sci Technol 2010;70(3):472–7.
[7] Clarke AR, Archenhold G, Davidson NC. A novel technique for determining the 3d spatial distribution of glass fibres in polymer composites. Compos Sci Technol 1995; 55(1):75–91.
[8] Blanc R, Germain C, Da costa JP, Baylou P, Cataldi M. Fiber orientation measurements in composite materials. Compos A Appl Sci Manuf 2006;37(2): 197–206.
[9] Salaberger Dietmar, Jerabek Michael, Koch Thomas, Kastner Johann. Consideration of accuracy of quantitative x-ray ct analyses for short-glass-fibre-reinforced polymers. Mater Sci Forum 2015;825–826:907–13.
[10] Wirjadi O, Schladitz K, Rack A, Breuel T. Applications of anisotropic image filters for computing 2d and 3d-fiber orientations. In: Stereology and image Analysis10th european congress of ISS; 2009.
[11] Daniels Florie, ter Haar Romeny Bart M, Rubbens M, Van Assen H. Quantification of collagen orientation in 3D engineered tissue. In: 3rd kuala Lumpur international conference on biomedical engineering 2006. Springer; 2007. p. 282–6.
[12] Krause M, Hausherr JM, Burgeth B, Herrmann C, Krenkel W. Determination of the fibre orientation in composites using the structure tensor and local x-ray transform. J Mater Sci 2010;45(4):888–96.
[13] Bertram Benjamin, Pinter Pascal. Composight. 2015.
[14] Müller Viktor, Brylka Barthel, Dillenberger Felix, Glöckner Robert, Kolling Stefan, Böhlke Thomas. Homogenization of elastic properties of short-fiber reinforced composites based on measured microstructure data. J Compos Mater 2016;50(3): 297–312.
[15] Kehrer Loredana, Pinter Pascal, Böhlke Thomas. Homogenization of temperature-dependent short fibre reinforced polypropylen and experimental investigations of long fibre reinforced vinylester. In: Proceedings in applied mathematics and Mechanics. Proceedings to 17th european conference on composite materials; 2016.
[16] Müller Viktor. Micromechanical modeling of short-fiber reinforced composites. 2016.
[17] Benveniste Y. A new approach to the application of mori-tanaka's theory in composite materials. Mech Mater 1987;6(2):147–57.
[18] Ken-Ichi Kanatani. Distribution of directional data and fabric tensors. Int J Eng Sci 1984;22(2):149–64.
[19] Schneider Matti. The sequential addition and migration method to generate representative volume elements for the homogenization of short fiber reinforced plastics. Comput Mech 2017;59(2):247–63.
[20] Weidenmann KA, Baumann S, Pinter P, Elsner P. Analysis of fiber orientation, microstructure and mechanical properties of specimens made from fiber-reinforced ABS manufactured by fused filament fabrication (FFF). In: Proceedings of the european conference on composite materials (ECCM17), vol. 06; 2016.
[21] Leopardi Paul. A partition of the unit sphere into regions of equal area and small diameter. Electron Trans Numer Anal 2006;25:p309–327.
[22] Jähne Bernd. Digitale Bildverarbeitung und Bildgewinnung. Springer-Verlag Berlin Heidelberg; 2012.
[23] Ibanez Luis, Schroeder Will, Ng Lydia, Cates Josh, the Insight Software Consortium. itk software guide. 2005.
[24] Mori Tanaka, Tanaka K. Average stress in matrix and average elastic energy of materials with misfitting inclusions. Acta Metall 1973;21(5):571–4.
[25] Kehrer L, Pinter P, Böhlke T. Mean and full field homogenization of artificial long fiber reinforced thermoset polymers. In: Proceedings in applied mathematics and Mechanics; 2017. submitted for publication.
[26] Böhlke T, Brüggemann C. Graphical representation of the generalized hookes law. Tech Mech 2001;21(2):145–58.
[27] Kapur JN, Sahoo PK, Wong AKC. A new method for gray-level picture thresholding using the entropy of the histogram. Comput Vis Graph Image Process 1985;29(3): 273–85.